


SCIENTIFIC REPORTS



OPEN

Understanding the effects of Cr doping in rutile TiO₂ by DFT calculations and X-ray spectroscopy

G. Cristian Vásquez^{1,2}, David Maestre¹, Ana Cremades¹, Julio Ramírez-Castellanos³, Elena Magnano⁴ & Silvia Nappini⁴, Smagul Zh. Karazhanov²

The effects of Cr on local environment and electronic structure of rutile TiO₂ are studied combining theoretical and experimental approaches. Neutral and negatively charged substitutional Cr impurities Cr_{Ti}⁰ and Cr_{Ti}¹⁻ as well as Cr-oxygen vacancy complex 2Cr_{Ti} + V_O are studied by the density functional theory (DFT) within the generalized gradient approximation (GGA) of Perdew-Burke-Ernzerhof (PBE) functional. Experimental results based on X-Ray absorption spectroscopy (XAS) and X-Ray photoelectron spectroscopy (XPS) performed on Cr doped TiO₂ at the Synchrotron facility were compared to the theoretical results. It is shown that the electrons of the oxygen vacancy tend to be localized at the *t*_{2g} states of the Cr ions in order to reach the stable oxidation state of Cr³⁺. Effects of Cr on crystal field (CF) and structural distortions in the rutile TiO₂ cell were analyzed by the DFT calculations and XAS spectra revealing that the CF and tetragonal distortions in TiO₂ are very sensitive to the concentration of Cr.

Due to many technologically important optical, electronic and mechanical properties transition metal oxides have attracted increased research attention during the last years. Their optical, electronic and mechanical properties are appropriate for a wide range of applications. Titania (TiO₂) is a semiconducting oxide that in both the anatase and rutile polymorphs have been applied in electronics, optoelectronics¹, sensors², photocatalysts^{3,4}, energy production and storage⁵, etc. Study of cationic dopants in TiO₂ is of great interest because it allows to modify and/or enhance physical and chemical properties of TiO₂, thus advance the respective device performance and extend its application range⁶⁻¹⁰. Transition metal impurities such as Cr, V, Mn or Fe, can be easily incorporated into TiO₂ lattice, which aroused interest since these dopants commonly improve physicochemical reactions at the surface that is important for degradation of pollutants in waste water treatment or in energy related applications where the oxidation state of the dopant plays a key role^{6,8,11}. Nevertheless, achieving a controlled oxidation state of the transition metals in TiO₂ is not a simple task, due to their characteristic multivalence. Many factors should be accounted for in the analysis of doping process, such as the temperature, atmosphere and precursors used during the synthesis, the dimensions and morphology of the material, and the final concentration of dopants, among others, which usually affect the position of the dopant in the lattice and its ground state nearby other intrinsic defects¹¹⁻¹³. Among the other transition metals, Cr has frequently been the matter of study because of the controversy related to its influence on the physical and chemical properties of TiO₂. As an example, Fan *et al.*³ observed that mesoporous Cr-doped TiO₂ presents lower photocatalytic activity for acetaldehyde photodecomposition under the UV light radiation and its performance varies as a function of the Cr concentration and the irradiation wavelength, generally increasing below the critical Cr doping level. Similar observations were reported by Wei *et al.*¹⁴, Tian *et al.*⁴ On the contrary, Wilke *et al.*⁶ and recently Mittal *et al.*¹⁵ did not observe any photocatalytic improvement by Cr doping despite higher visible light absorption was reported. The magnetic properties of Cr doped TiO₂ has been also investigated due to potential applications for spintronics and novel information processing¹⁶. In contrast to non-magnetic TiO₂ observed by Matsumoto *et al.*¹³, ferromagnetic behavior at room temperature has been observed by other authors, however the variables involved in the magnetic properties are still unclear and remains under debate^{9,16,17}. Therefore, a deeply understanding of electronic structure of doped

¹Departamento de Física de Materiales, Facultad de CC. Físicas, Universidad Complutense, 28040, Madrid, Spain.

²Department for Solar Energy, Institute for Energy Technology, 2007, Kjeller, Norway. ³Departamento de Química Inorgánica I, Facultad de CC. Químicas, Universidad Complutense, 28040, Madrid, Spain. ⁴IOM-CNR, Laboratorio TASC, S.S. 14-km 163.5, 34149, Basovizza, Trieste, Italy. Correspondence and requests for materials should be addressed to G.C.V. (email: gc.vasquez@ucm.es)

Sample	Form	Concentration [cat.% Cr]
TiO ₂ -np(R)	Nanoparticles	0.0
Cr02	Microtubes	1.8 ± 0.2
Cr03	Microtubes	2.8 ± 0.3
Cr04	Sintered	4.0 ± 0.3
Cr05	Nanoparticles	5.0 ± 0.4
Cr ₂ O ₃ Ref.	Polycrystalline	—

Table 1. List of samples and corresponding Cr concentration in cationic fraction respect to Ti quantified by EDS.

systems like TiO₂ is still needed, and the parameters such as the dopant oxidation state and the site where the dopant is located in the host lattice, as well as the influence of the dopant on the oxygen related defects should be further investigated in order to understand the dopant-induced physical and chemical effects¹⁸.

The present study focuses on modifications of electronic structure of rutile TiO₂ induced by the incorporation of Cr, paying attention on the Cr oxidation state, location in the lattice, on formation of complex with oxygen vacancies, on its influence on lattice environment, and on its shallow ionization energy in the band gap. The aim of this work is combine theoretical and experimental studies of Cr-doped TiO₂ samples, in order to shed light on the effects caused by doping in a wide range of concentrations that may affect their optoelectronic properties. Density functional theory (DFT) based calculations were carried out to investigate the effect of Cr on electronic density of states (DOS) of ideal and oxygen-deficient crystalline TiO₂. The electronic structure has been experimentally studied by resonant and non-resonant X-ray Photoelectron Spectroscopy (XPS) and X-ray Absorption Spectroscopy (XAS) performed at a Synchrotron beamline that have been compared to the above theoretical results. The morphological and crystalline characteristics of the present microstructures, as well as the doping homogeneity achieved, make them an useful reference material for theoretical studies of Cr-doped TiO₂. Moreover, this study could serve as a reference model for other metallic oxides that also crystallize in the rutile-like structure such as VO₂, CrO₂, MnO₂, SnO₂ or RuO₂.

Experimental Section

Samples studied. The Cr-doped rutile TiO₂ microtubes analyzed in this work have been synthesized by a vapor-solid method at temperatures of 1300 °C during 15 h, using 5 cat.% and 10 cat.% Cr-doped nanoparticles as precursor, as reported in a previous work¹⁹. These microtubes exhibit high crystallinity and chromium homogeneity, up to 3–4 cat.% Cr. A combined Raman spectroscopy in a confocal microscope and electron back scattered diffraction (EBSD) in a SEM¹⁹ confirm the growth direction and the lateral planes forming the tubes, which correspond to the [001] direction and the {110} family planes, respectively. These techniques also revealed the high crystalline quality of the microtubes, which lateral faces can be considered as single-crystals. In addition, undoped rutile TiO₂ and Cr doped samples up to 5 cat.% Cr have been analyzed for comparison and commercial α -Cr₂O₃ polycrystalline powder (Sigma Aldrich, 99.9%), were employed as reference samples. Table 1 summarizes the samples used in this work and their Cr content.

Characterization. XAS experiments in total electron yield (TEY) mode, as well as resonant and non-resonant XPS measurements were carried out at the BACH beamline at the Elettra Synchrotron light source facility (Trieste, Italy) using a monochromatic photon energy in the range from 400 to 600 eV, with energy resolution of 40–200 meV. The spectra were acquired in normal incidence geometry. C(1 s) peak at 284.6 eV from adventitious carbon²⁰ has been employed for calibration of the XPS spectra. Chromium quantification was performed by energy dispersive spectroscopy (EDS) with a Bruker AXS 4010 detector mounted in a Leica 440 SEM.

DFT Calculations. All the calculations were performed using the density functional theory (DFT) implemented in the Vienna *ab initio* simulation package (VASP)^{21–23} together with the potential projector augmented-wave (PAW) method^{24–26}. The core and valence electronic states are expanded with a plane-wave basis set, with an optimal energy cutoff of 500 eV. Standard PAW-PBE²⁷ pseudopotentials were employed to describe the Ti(3s3p3d4s), Cr(4s3p3d) and O(2s2p) valence states, allowing spin polarization during all calculations.

The defect calculations were performed using a 2 × 2 × 4 (96 atoms) supercell for the neutral and negative charged Cr defects (Cr_{Ti}⁰, Cr_{Ti}¹⁻) and also for the combined neutral defect 2Cr_{Ti}⁰ + V_O⁰. A 4 × 4 × 6 mesh for the *k*-point sampling centered at the Gamma point was found optimal for the calculations. Additionally, calculations using hybrid functional with a 25% portion of Hartree-Fock exchange using the standard HSE06²⁸ screening parameter of 0.2 Å⁻¹ were performed to analyze the 2Cr_{Ti}⁰ + V_O⁰ case using a 2 × 2 × 2 supercell and a 2 × 2 × 2 mesh for the *k*-point sampling. The structural optimization for point defects in the supercell were performed starting from a pre-converged unit cell and allowing ionic relaxation with energy convergence of 10⁻⁷ eV per atom and minimizing the forces on all atoms less than 10⁻² eV·Å⁻¹. The calculation of the effective charges were performed using the Henkelman's grid-based algorithm for the Bader electron decomposition method²⁹. The effective charge is defined as $Q_X = Z_X - q_{\text{Bader},X}$ (X = Cr, Ti, O) similar to that calculated in Vasquez *et al.*³⁰, where Z_X is the number of valence electrons and $q_{\text{Bader},X}$ is the calculated Bader charge for the corresponding X atom. Graphical illustrations were drawn using the software VESTA³¹.

	a [Å]	c [Å]	d_0 [Å]	D_0 [Å]	E_g [eV]	Q_{Ti} [e]	Q_O [e]
PBE ^a	4.65345	2.97300	1.96418	2.00662	1.8	+2.23	-1.12
HSE ^a	4.59042	2.95413	1.94500	1.98050	3.2	+2.43	-1.21
Experimental ^b	4.5937	2.9587	1.946	1.984	3.0–3.1		
PBE ^c	4.650	2.971		2.006	1.77	+2.22	-1.12
HSE ^c	4.590	2.947		1.980	3.05		
LDA ^c	4.557	2.929			1.79		

Table 2. List of lattice parameters, bond lengths, energy band gap and Bader effective charge calculated for the rutile phase. Comparison to experimental data and other theoretical studies are included. ^aPrevious work (ref.³⁰); ^bref.^{39,48–50}; ^cref.^{33,44,51}.

	D_0 [Å]	d_0 [Å]	$ D-d /D$ [%]	$Q_{Cr,Ti}$ [e]
Cr_{Ti}^{1-}				
CrO ₆	1.998	1.987	0.55	+1.75
TiO ₆	2.008	1.964	2.24	+2.23
Cr_{Ti}^0				
CrO ₆	1.939	1.943	0.21	+1.93
TiO ₆	2.009	1.965	2.24	+2.23

Table 3. List of apical (D) and basal (d) bond length in CrO₆ and TiO₆ octahedra, $|D-d|/D$ percentages, and Bader effective charge for Cr and Ti ions for Cr_{Ti}^{1-} and Cr_{Ti}^0 defects in rutile.

Results and Discussion

DFT study. Substitution of a single Ti atom by a Cr atom in the $2 \times 2 \times 4$ rutile supercell corresponds to cationic concentration of ~ 3.1 cat.% Cr in good agreement with that measured by EDS in the studied Cr doped rutile microtubes¹⁹. The neutral Cr_{Ti} in ideal TiO₂ lattice leads to Cr^{4+} ion, whereas the negatively charged Cr_{Ti}^{1-} defect corresponds to Cr^{3+} ion. Both cases and the defect-impurity complex $2Cr_{Ti} + V_O$ are studied in this work and are compared to our experimental data obtained by XPS and XAS measurements.

The rutile structure is formed by an infinite chain of TiO₆ octahedra with four basal (d_0) and two apical (D_0) Ti-O bond lengths. The basal bonds form an angle of 98.8° whereas the apical bonds form a right angle with respect to the basal plane³². Therefore, each octahedron is slightly tetragonal and trigonal distorted. In a previous work³⁰ we have compared electronic properties of bulk rutile as calculated by PBE and hybrid functional (HSE06), as well as the effect of V_O^{2+} on the TiO₂ lattice and conduction band, so the complete list of rutile TiO₂ parameters, as well as our experimental values and data from other authors, are summarized in the Table 2.

Our results are in good agreement with those commonly reported by other authors. Small differences, below 1%, are found between the results obtained from the calculations obtained within PBE and HSE. Large differences are found in the calculated band gap (E_g), which is underestimated by the PBE method. Janotti *et al.*³³ reported that this effect in rutile TiO₂ can be attributed to a reduced self-interaction for the O(2p)-derived states at the upper part of the valence band. Bader charge analysis calculated by HSE06 indicates a slightly higher ionic character in the Ti-O bond as compared with the PBE calculations³⁰. Taking into account that, apart from E_g underestimation by the PAW-PBE functional, comparable values are obtained by both computational methods, in this work the PBE method has been employed in most of the analyzed simulations, as it allows to spread the type of defects to be simulated while keeping calculation time lower than HSE06.

After the ionic relaxation we have observed that the symmetry of the CrO₆ octahedron incorporated in TiO₂ is different as compared to the TiO₆ octahedron, which shows both tetragonal and trigonal distortions. In Table 3 the PBE calculated data for apical (D) and basal (d) Cr-O and Ti-O bond lengths in CrO₆ and TiO₆ octahedra are indicated for both Cr_{Ti}^{1-} and Cr_{Ti}^0 defects in rutile TiO₂.

In addition, the corresponding $(D-d)/D$ percentages and the calculated Bader effective charge values are also included in Table 3. In the case of the CrO₆ octahedron, the tetragonal distortion is significantly reduced, where the relative difference between calculated apical (D) and basal (d) Cr-O bond length is less than 0.55% in comparison to the value obtained for Ti-O bonds of 2.4%. This observation indicates that the Cr ion symmetry in rutile TiO₂ is nearly octahedral (O_h) rather than tetragonal distorted octahedral symmetry as the TiO₆ octahedron in perfect rutile.

Bader charge analysis as a function of the distance from the Cr_{Ti} defect, either for Cr_{Ti}^{1-} or Cr_{Ti}^0 , shows very small dispersion in effective charge values for O and Ti atoms as observed in the Fig. 1, which means that in both cases the electronic charge around the defect is very localized in the Cr atom. Only the nearest O atoms (ca. 2 Å), which are directly bonded to Cr, present small variations in the effective charge. Dots above the dotted line (reference from bulk TiO₂) in Fig. 1(b,d) indicate that the O atoms coordinated with the corresponding Cr defect gain less charge than those O atoms only coordinated with Ti atoms in bulk rutile. Thus, the number of valence electrons in the different Cr defects (Cr_{Ti}^{1-} , Cr_{Ti}^0) influences the Cr-O bonding, as expected. The Cr d -orbital is occupied by two electrons in the case of a Cr^{4+} ion (Cr_{Ti}^0 defect), and three in the case of a Cr^{3+} ion (Cr_{Ti}^{1-}). This implies that the additional electron in the Cr_{Ti}^{1-} defect belongs to the Cr valence electrons, expanding slightly the octahedron volume by increasing the Cr-O bond length (see Table 3).

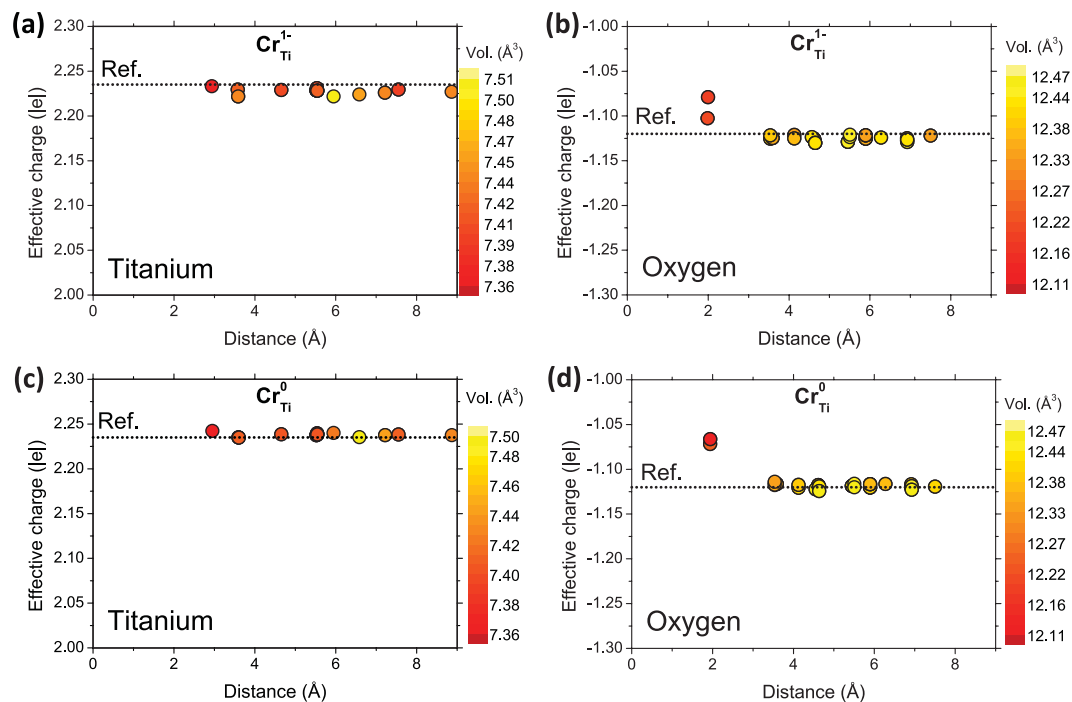


Figure 1. Bader effective charge as a function of the distance from the Cr defect for (a) Titanium atoms and (b) Oxygen atoms in $\text{Cr}_{\text{Ti}}^{1-}$ defect, and (c) Titanium atoms and (d) Oxygen atoms in Cr_{Ti}^0 . Dotted line represents the Bader charge for bulk rutile.

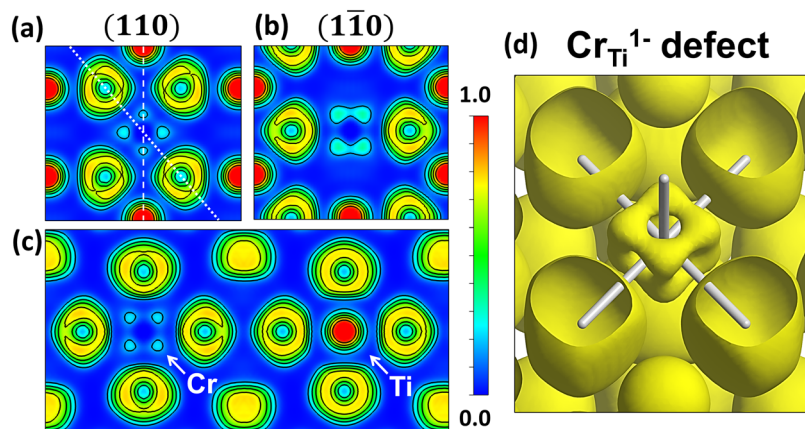


Figure 2. ELF cross section along the (a) (110) plane, (b) $(1\bar{1}0)$ plane and (c) the apical plane perpendicular to (110) for the $\text{Cr}_{\text{Ti}}^{1-}$ defect. Dotted line in (a) represents the intersection with $(1\bar{1}0)$ plane and dashed line represents the intersection with the apical plane. (d) Isosurface for an $\text{ELF} = 0.15$ for the $\text{Cr}_{\text{Ti}}^{1-}$ defect. Cr–O bonds are represented as white sticks.

More differences can be appreciated by the observation of the electronic distribution by means of the electron localization function (ELF), corresponding to both types of Cr defects. In Fig. 2(a,b) the ELF basal cross-section planes for the rutile (110) and $(1\bar{1}0)$ planes, respectively, are represented for the case of $\text{Cr}_{\text{Ti}}^{1-}$. The $(1\bar{1}0)$ plane is perpendicular to (110) plane crossing along the dashed line marked in Fig. 2(a), where the $\text{Cr}_{\text{Ti}}^{1-}$ defect is located at the center. Figure 2(c) corresponds to the apical plane crossing along the dotted line of the Fig. 2(a). The equivalent cross-section planes corresponding to the Cr_{Ti}^0 defect in rutile TiO_2 are represented in Fig. 3.

In both cases the electron density around the basal Cr–O bonds [Figs 2(a) and 3(a)] is practically negligible in the (110) planes, and in a greater extent for the $\text{Cr}_{\text{Ti}}^{1-}$ defect. However, the apical bonds are different depending on the Cr oxidation state. For the neutral Cr_{Ti}^0 defect (Cr^{4+}) the ELF value is higher in the apical Cr–O bonds, contrary to $\text{Cr}_{\text{Ti}}^{1-}$ (Cr^{3+}) where the electron density is still minimum as can be observed in Figs 2(b) and 3(b), corresponding to the $(1\bar{1}0)$ planes. The trigonal distortion in the (110) plane modifies the electron density, thus increasing the ELF value in the regions where O–Ti–O angle is $>90^\circ$, unlike the apical plane represented in the Figs 2(c) and 3(c) where all the Cr–O bonds are nearly equivalent and the plane is unaffected by octahedral

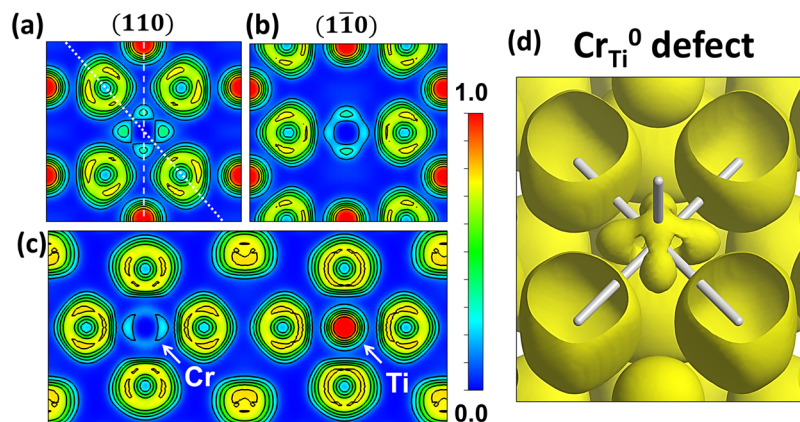


Figure 3. ELF cross section along the (a) (110) plane, (b) ($1\bar{1}0$) plane and (c) the apical plane perpendicular to (110) for the Cr_{Ti}^0 defect. Dotted line in (a) represents the intersection with ($1\bar{1}0$) plane and dashed line represents the intersection with the apical plane. (d) Isosurface for an ELF = 0.15 for the Cr_{Ti}^0 defect. Cr–O bonds are represented as white sticks.

distortions. The isosurfaces for an ELF value of 0.15 corresponding to the $\text{Cr}_{\text{Ti}}^{1-}$ and Cr_{Ti}^0 defects are shown in the Figs 2(d) and 3(d), respectively. The Cr–O bonds are represented as white sticks. All the features described for the ELF cross-sectional views can be appreciated in the volumetric space in Figs 2(d) and 3(d). In this way, the electron density around $\text{Cr}_{\text{Ti}}^{1-}$ defect is distributed forming a cube-like volume, whereas the electron localization around the Cr_{Ti}^0 defect shows a more complex distribution with localized electrons in the regions around the apical bonds. The relatively small difference in the effective charges between the $\text{Cr}_{\text{Ti}}^{1-}$ and Cr_{Ti}^0 defects (Table 3) combined with the ELF results suggest that the Cr–O bonding character is mostly ionic in the case of a $\text{Cr}_{\text{Ti}}^{1-}$ defect, whereas the apical Cr–O bonds in the Cr_{Ti}^0 defect present a covalent character slightly higher than Ti^{4+} in TiO_2 . Thereby, the different number of valence electrons affects differently to the electron distribution in each Cr defect. The characteristic ELF of the $\text{Cr}_{\text{Ti}}^{1-}$ defect could be explained as valence electrons that tend to occupy the d_{xy} , d_{yz} and d_{zx} orbitals, pointing to directions between Cr–O bonds, instead of the d_{z^2} and $d_{x^2-y^2}$ orbitals which are pointing towards the coordinated O atoms. This suggests that the electron configuration in the ground state of $\text{Cr}_{\text{Ti}}^{1-}$ defect is $3t_{2g}^3e_g^0$ characteristic of an Cr^{3+} ion under octahedral (O_h) crystal field. In the case of the Cr_{Ti}^0 , the higher electron localization along the apical bonds indicates that the electrons can partially occupy the d_{z^2} orbitals.

In order to complete the DFT study, the density of electronic states (DOS) has also been analyzed. The total DOS and partial DOS (pDOS), including O(2p), Ti(3d) and Cr(3d), for the $\text{Cr}_{\text{Ti}}^{1-}$ and Cr_{Ti}^0 defects in rutile TiO_2 are shown in Fig. 4(a). For clarity, the VBM is set to 0 eV, and s^+ and s^- indicate the spin-up and spin-down components of the DOS, respectively.

The pDOS reveals that the Cr defect states within the TiO_2 band gap are originated by orbitals of Cr 3d nature. With regard to the $\text{Cr}_{\text{Ti}}^{1-}$ defect [top of the Fig. 4(a)], the occupied electronic states are localized as a spin-up level 0.2 eV below the E_F and about 0.75 eV above the VBM. The neutral Cr_{Ti}^0 defect [down in the Fig. 4(a)] shows electronic states partially occupied within the E_g with a symmetric state below the E_F and a more complex defect structure with spin-up and spin-down polarized states at the CB region. Figure 4(b) shows the partial contribution of O(2p) and Cr(3d) orbitals for CrO_6 octahedron compared with a single TiO_6 octahedron (dashed line) for both $\text{Cr}_{\text{Ti}}^{1-}$ and Cr_{Ti}^0 . In the case of $\text{Cr}_{\text{Ti}}^{1-}$ [top of the Fig. 4(b)] the calculated VB contributions of the CrO_6 octahedron are similar to the calculated contributions for the TiO_6 octahedron. Within the band gap region, the O(2p) orbitals are slightly hybridized with Cr(3d) orbitals (t_{2g} related states) in the $\text{Cr}_{\text{Ti}}^{1-}$ defect. On the contrary, for the Cr_{Ti}^0 defect [down in Fig. 4(b)], the O(2p) and Cr(3d) orbitals show stronger hybridization states at about 5.2 eV below the E_F partially overlapped with the O(2p)- σ bonds of TiO_2 ³⁴. In the conduction band (CB) the Cr contributions are partially mixed with the empty t_{2g} states of the TiO_2 CB³³, showing localized states at about 3 eV above the E_F . Hereinafter our analysis will be focused on the VB region, thus results comparing the PAW-PBE and HSE06 functional are shown in Supplementary Fig. S1 confirming that the VB region are qualitatively similar using both functionals.

Other way to obtain Cr^{3+} defects in a neutral rutile lattice could be achieved by the electron transfer from neutral oxygen vacancies, V_O^0 , or ionized V_O^{n+} defects ($n = 1, 2$), to nearby Cr^{4+} defects. To perform and simulate this possibility, a single V_O^0 is created in the proximity of two Cr_{Ti}^0 defects resulting in the combined defect $2\text{Cr}_{\text{Ti}} + \text{V}_O$ studied in this work. Figure 5(a) shows the ELF cross section for the (110) plane calculated by PBE for the combined defect $2\text{Cr}_{\text{Ti}} + \text{V}_O$. The dotted lines indicate broken Cr–O and Ti–O bonds due to the removed oxygen atom (V_O).

After ionic relaxation, the trapped electrons from the removed O atom are localized in the region between the Cr and Ti dangling d orbitals. The presence of the V_O defect generally results in displacements of the Ti and O atoms outward and inward, respectively, from the V_O site^{30,33,35}. In the combined defect, the Cr atoms [Cr(1) and Cr(2) in Fig. 5(a)] are displaced outward from the V_O^0 , but only a small amount ($1.04d_0$) as compared to the nearest Ti atoms from the V_O^{2+} defect ($1.16d_0$ from Janotti *et al.*³³). However, the next nearest Ti atom [Ti(1) in

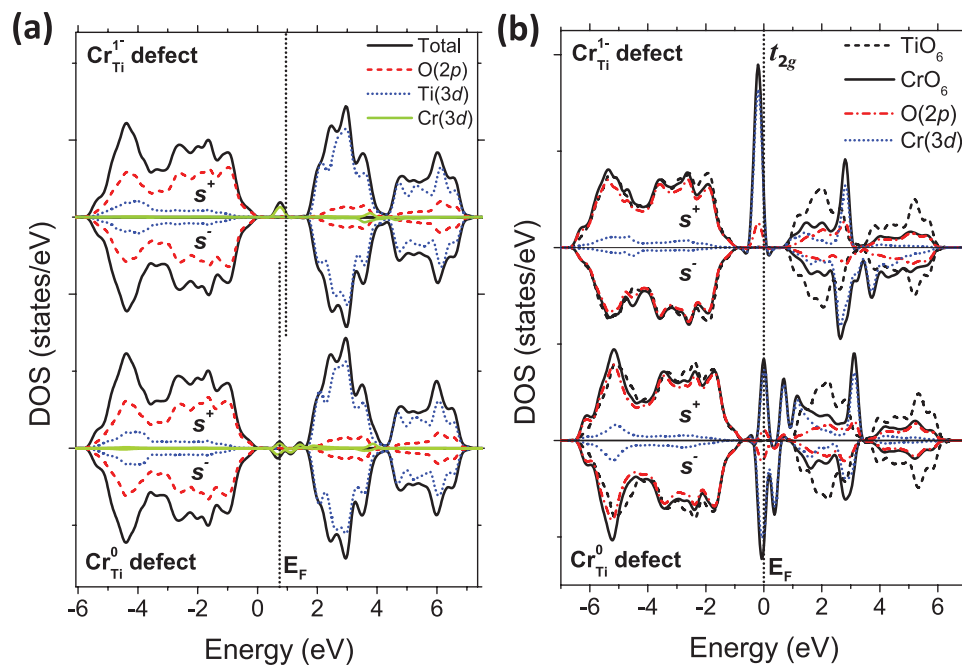


Figure 4. (a) Spin polarized (s^+ , s^-) total DOS and pDOS corresponding to O(2p), Ti(3d) and Cr(3d) states for $\text{Cr}_{\text{Ti}}^{1-}$ and Cr_{Ti}^0 defects, and (b) DOS contributions from CrO_6 and TiO_6 (dashed) octahedra.

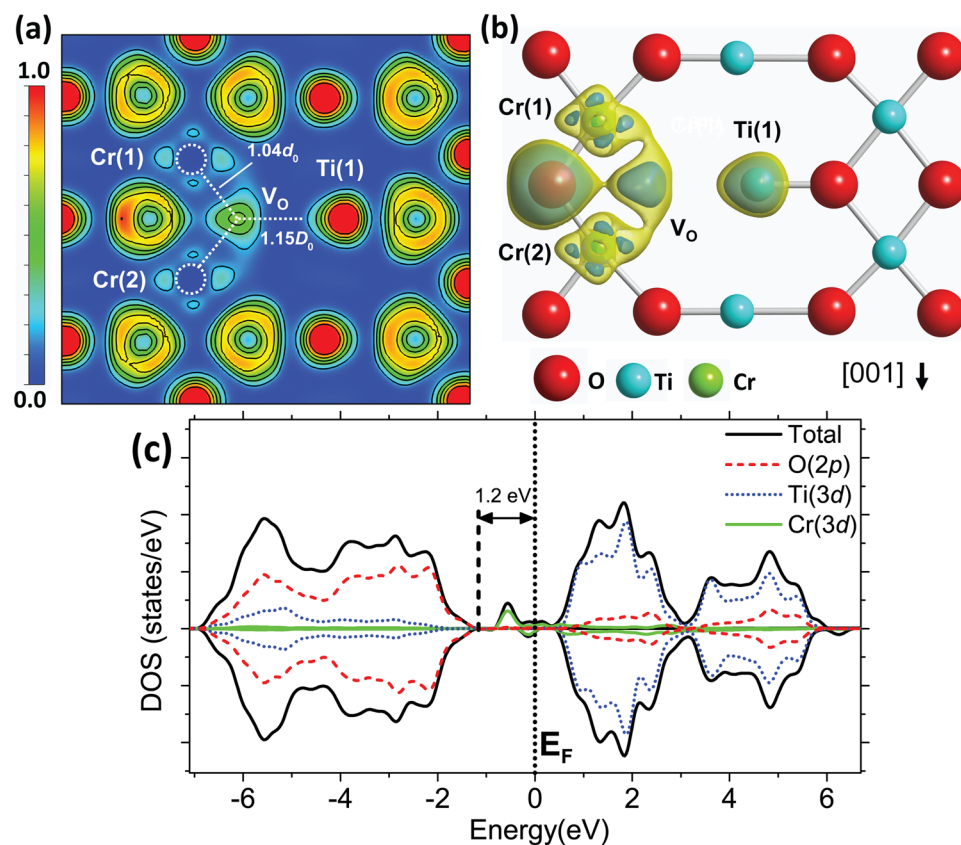


Figure 5. (a) ELF cross section along the (110) plane with a combined $2\text{Cr}_{\text{Ti}}^0 + V_O^0$ defect. Dotted circles and lines represent the Cr atoms and dangling bonds, respectively. (b) ELF isosurfaces for an ELF value of 0.11 (yellow/light) and 0.21 (blue/dark) around the nearest Cr, Ti and O atoms from the V_O defect. (c) Spin polarized (s^+ , s^-) total DOS and pDOS corresponding to O(2p), Ti(3d) and Cr(3d) states for the combined $2\text{Cr}_{\text{Ti}}^0 + V_O^0$ defect.

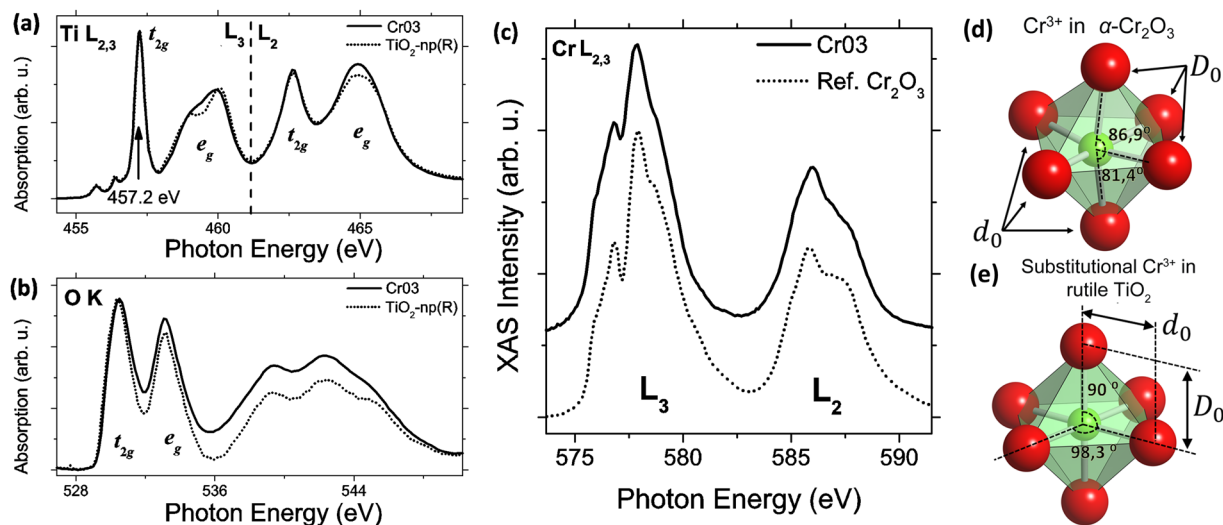


Figure 6. (a) XAS spectra from Ti- $L_{2,3}$ edge, (b) O-K edge and (c) Cr- $L_{2,3}$ edge. (d) CrO_6 octahedron from $\alpha\text{-Cr}_2\text{O}_3$ and (e) $\text{Cr}_{\text{Ti}}^{3+}$ defect in rutile TiO_2 .

Fig. 5(a)] is displaced an amount of about $1.15D_0$, equivalent to that calculated for V_O^{2+} ($1.15D_0$ from Janotti *et al.*³³). Despite the fact that charge density in the bonded O atom [between Cr(1) and Cr(2) in the Fig. 5(a)] is repelled outward from the vacancy site, observed as a high electron localization in the opposite side from the V_O , only small distortions can be observed around Cr atoms because of the ionic relaxation as compared to single V_O^{2+} . The isosurfaces represented in the Fig. 5(b) for ELF values of 0.11 (in yellow/light) and 0.21 (in blue/dark) show that electron localization geometry around Cr atoms is similar to that observed for the $\text{Cr}_{\text{Ti}}^{1-}$ defect [Fig. 2(d)]. Therefore, the electron localization is also characteristic for Cr^{3+} ions. However, in this case the electrons from the V_O state are bounded with Cr atoms indicating the presence of a mixed $\text{Cr}(3d)\text{-V}_\text{O}$ electronic state. The Total DOS and pDOS corresponding to O($2p$), Ti($3d$) and Cr($3d$) states for the combined defect $2\text{Cr}_{\text{Ti}} + \text{V}_\text{O}$ are represented in Fig. 5(c). It can be noticed that DOS shape is similar to that calculated for the $\text{Cr}_{\text{Ti}}^{1-}$ defect [top in Fig. 4(b)] characterized by spin-up polarized defect states of $\text{Cr}(3d)$ nature at about 0.75 eV above the VBM. For the combined defect there are also partially occupied states close to the E_F which increase the energy splitting between the VBM and the E_F from 0.95 eV, for $\text{Cr}_{\text{Ti}}^{1-}$, to 1.2 eV, for the combined $2\text{Cr}_{\text{Ti}} + \text{V}_\text{O}$. In this case the electronic states of the V_O^0 are mixed with the nearest Cr t_{2g} orbitals resulting in a high spin polarized state, similar to that observed for the $\text{Cr}_{\text{Ti}}^{1-}$, which means that electrons from V_O contribute to the formation of a pair of Cr^{3+} defects.

XPS and XAS study. XAS and XPS measurements have been performed at BACH beamline at the Elettra synchrotron facility in order to investigate the electronic structure and the effect of Cr in rutile TiO_2 . The combination of these experimental results with the theoretical study will extend the understanding of the Cr doping process in rutile TiO_2 . In this way, XAS spectra have been acquired on the Cr doped microtubes, as well as on undoped TiO_2 and Cr_2O_3 reference samples. The Fig. 6(a–c) show the XAS spectra from Ti- $L_{2,3}$, O-K and Cr- $L_{2,3}$ absorption edges, respectively, from the doped CrO3 microtubes. Spectra from undoped TiO_2 and Cr_2O_3 are also included for comparison. The Ti- $L_{2,3}$ edge is splitted in two regions due to the spin-orbit coupling forming the L_3 and L_2 edges, as marked in Fig. 6(a).

Both L_3 and L_2 bands are subdivided in two contributions as a result of the crystal field (CF), that originates the fivefold d -orbital splitting into two degenerated levels of t_{2g} (three-fold degenerate states) and e_g (two-fold degenerate states) symmetry by an energy amount of $10Dq$ eV, also known as CF splitting³⁶. According to the atomic coordinates calculated by DFT, TiO_6 octahedron in the rutile phase presents both trigonal and tetragonal distortions. TiO_2 tetragonal distortions, affecting directly to apical Ti–O bonds, are more sensitive in the $L_{2,3}$ -edge. Under tetragonal distortion the e_g states are splitted in two states of b_{1g} and a_{1g} symmetry, whereas t_{2g} states are splitted in three states of b_{2g} and e_g (two-fold degenerated) symmetry³⁷. The high energy resolution achieved in the acquisition of the XAS spectra (<0.1 eV) enables the observation of the e_g splitting at the L_3 edge, resulting in the characteristic rutile TiO_2 fingerprint with a maximum at 460 eV and a shoulder around 459 eV^{32,37}, as observed in Fig. 6(a). Analogously, this association can be extended to the L_2 edge, although the absorption bands in the latter region are broader because of Auger decay effects and vibrational dispersions³⁸. It can be noticed that in Fig. 6(a) the e_g band presents slight, but not negligible, modifications in Cr doped samples such as a less defined e_g splitting at the L_3 edge or variations in the e_g relative intensity at the L_2 edge.

On the other hand, the O-K edge [Fig. 6(b)], corresponding to electronic transition $1s \rightarrow 2p$, also shows features that are sensitive to the crystal environment. The hybridization of the Ti($3d$)–O($2p$) orbitals in TiO_2 makes able the observation of the t_{2g} and e_g bands in the O-K edge³², observed at 530 and 533 eV, respectively. Complex contributions at higher energies with two maxima at 539 and 542 eV and a shoulder at around 545 eV, are also characteristic of the rutile phase of TiO_2 ³⁹. In this case variations related to the e_g relative intensity can be observed in Fig. 6(b), similar to that observed at the L_2 edge in Fig. 6(a).

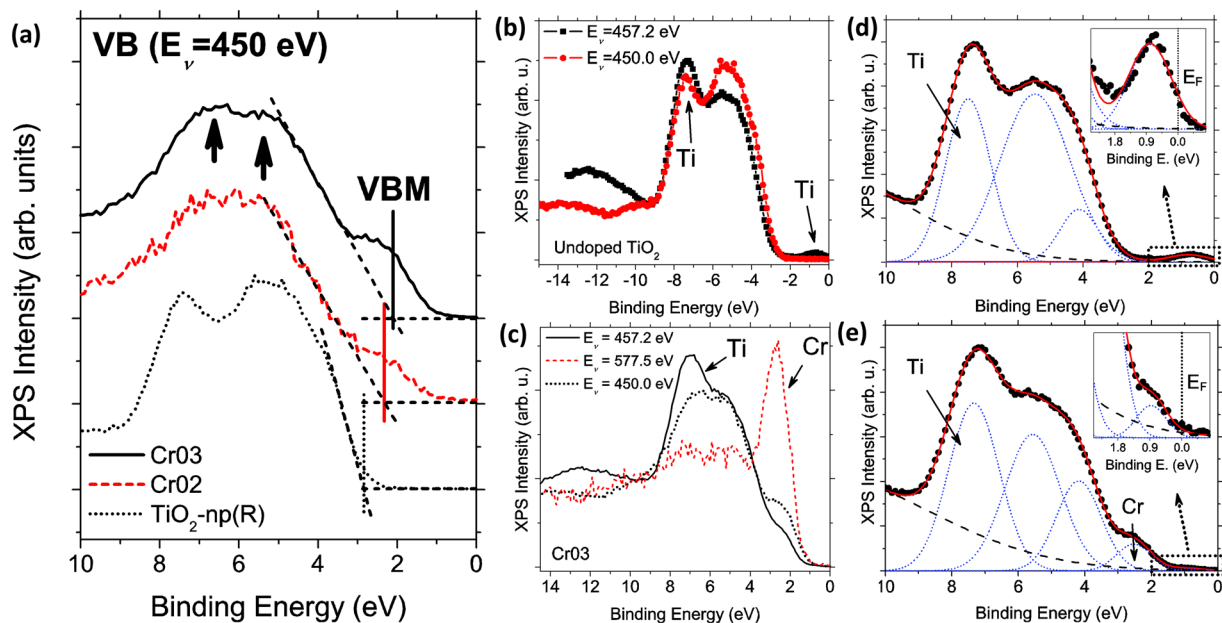


Figure 7. (a) VB-XPS spectra from undoped ($\text{TiO}_2\text{-np(R)}$) and Cr doped TiO_2 with different Cr concentration (CrO2, CrO3) using a photon energy $E_\nu = 450$ eV. The dashed lines are indicative for the estimation of the VBM. (b) On and off-resonance BV spectra from undoped TiO_2 and (c) Cr-doped TiO_2 microtubes (CrO3). Arrows in (b) and (c) mark the resonant peaks according to the absorption maximum selected. (d) Gaussian deconvolution (straight line) of Ti resonant XPS spectra (dots) measured with a photon energy of 457.2 eV for $\text{TiO}_2\text{-np}$ sample, and (e) Cr doped TiO_2 (CrO3). The insets in (d) and (e) correspond to enlargement of the E_F region.

The Cr $L_{2,3}$ edge [Fig. 6(c)] shows a more complex structure. The number of allowed transitions is significantly greater for the Cr atom due to the partially filled d orbitals in the case of Cr^{3+} or Cr^{4+} oxidation states, making difficult the analysis of the Cr-L edge. Thus, the Cr- $L_{2,3}$ edge from an $\alpha\text{-Cr}_2\text{O}_3$ sample has been used as a reference and compared to the Cr- $L_{2,3}$ from CrO3 microtubes. The main features in the corresponding XAS spectra in Fig. 6(c), as the maxima at 576.6 and 577.5 eV, or the spin-orbit energy splitting ($L_3\text{-}L_2$ separation), indicate that the most probable oxidation state in the Cr doped TiO_2 microtubes is Cr^{3+} under octahedral coordination, in agreement with previous CL results^{11,19}. However, the characteristic spectral features could be associated with the different octahedral distortions or local environment, as can be observed from the ball and stick diagrams for a CrO_6 unit from $\alpha\text{-Cr}_2\text{O}_3$ [Fig. 6(d)] and the calculated CrO_6 octahedron for a Cr^{3+} defect in rutile TiO_2 [Fig. 6(e)].

XPS spectra at the VB region (VB-XPS) from microtubes with different amount of Cr (see Table 1 in Experimental Section) have been analyzed, in addition to an undoped TiO_2 sample used as a reference. VB-XPS spectra acquired with energy of 450 eV are shown in Fig. 7(a).

Changes in the VB region can be observed as a function of the Cr doping. The undoped sample used as reference [dotted line in Fig. 7(a)] shows a VB-XPS spectrum with a broad band centered at 6 eV composed by two contribution with maxima located at 7.4 and 5.3 eV.

These contributions, attributed to $\text{O}(2p)\text{-}\sigma$ and $\text{O}(2p)\text{-}\pi$ states that are partially hybridized with $\text{Ti}(3d)$ ^{34,40}, can be also observed, although less defined, in the Cr doped samples CrO2 and CrO3 [marked with arrows in Fig. 7(a)]. In Cr doped TiO_2 , the VB is composed by a broad band, wider than that from undoped TiO_2 , centered at about 6 eV that extends approximately from 9 to 1 eV. Moreover, a shoulder close to the VBM, around 2.5–2.6 eV, is observed differently from the undoped TiO_2 . This band can be attributed to $\text{Cr}(3d)$ states¹⁰, as it is higher as the amount of Cr increases. At the same time, the VBM shifts towards the E_F as the amount of Cr increases in the microtubes, which should involve a less n -type behavior because of Cr doping at the surface of the probed microtubes.

Resonant XPS helps for the identification of valence states from Ti and Cr species. Figure 7(b) and (c) show the VB-XPS spectra acquired using photon energies corresponding to absorption maxima measured for Ti and Cr, according to their $L_{2,3}$ absorption edge spectra [Fig. 6(a,c)]. Figure 7(b) shows the VB spectra for undoped TiO_2 ($\text{TiO}_2\text{-np}$) using a photon energy off-resonance ($E_\nu = 450$ eV) and on-resonance ($E_\nu = 457.2$ eV). The XPS signal from Ti states in the VB increases under on-resonance conditions, showing peaks at 7.3 eV and 0.7 eV below E_F , marked with arrows in Fig. 7(b). The photoemission band at 7.3 eV is associated to hybridized $\text{O}(2p)\text{-Ti}(3d)$ σ -bonding states^{34,40}, whereas the band at 0.7 eV is associated to $\text{Ti}(3d)$ states as the result of reduced Ti^{3+} ions due to presence of oxygen vacancies and structural defects^{33,35}. The same experiment was carried out for Cr doped microtubes (CrO3), as shown in Fig. 7(c). In this case, a peak with a maximum at 7.0 eV is observed by using a photon energy on-resonance for Ti ($E_\nu = 457.2$ eV) which can be also related to $\text{O}(2p)\text{-Ti}(3d)$ hybridized states. However, selecting a photon energy on-resonance for Cr ($E_\nu = 577.5$ eV) a peak at 2.7 eV clearly dominates the

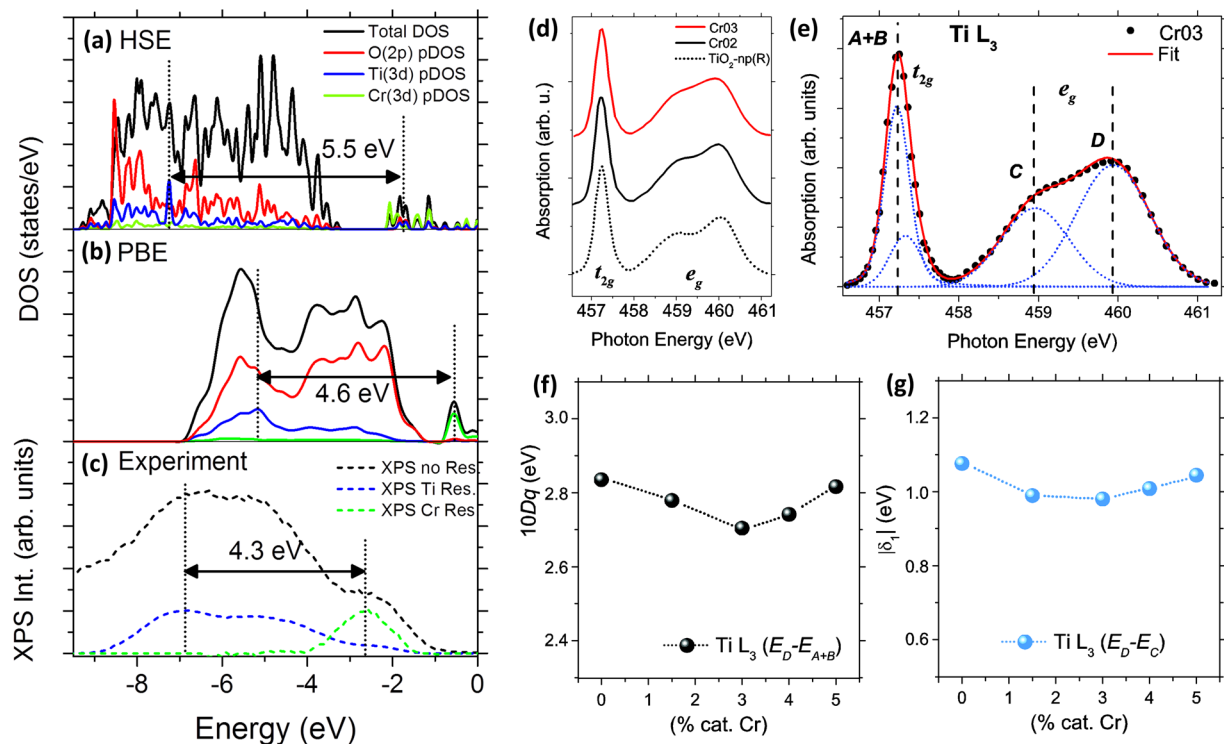


Figure 8. Comparison of the calculated DOS for $2\text{Cr} + \text{V}_\text{O}$ defect calculated by (a) HSE functional, (b) PBE and (c) the experimental VB spectrum (Cr03 sample). The intensity of the on-resonance spectra in (c) are reduced to obtain similar features. (d) Ti- L_3 spectra from undoped and Cr doped TiO_2 samples (Cr02 and Cr03). (e) Example of a Gauss-Lorentz (G-L) deconvolution of the Ti- L_3 edge. (f) Estimation of $10Dq$ parameter as a function of the Cr concentration from band deconvolution of Ti- L_3 edge. (g) Tetragonal distortion parameter $|\delta|$ as a function of the Cr concentration.

VB spectrum. This band at 2.7 eV was previously observed as a shoulder near the VBM in all the VB-XPS spectra measured for Cr doped samples [Fig. 7(a)], confirming that this contribution is related to Cr(3d) states¹⁰.

Figures 7(d,e) show the Gaussian deconvolution of the VB spectra in Fig. 7(b,c) acquired on-resonance for Ti atoms for undoped TiO_2 -np and Cr03 samples, respectively. The insets of the Fig. 7(d,e) show enlargement of the E_F region. In the undoped sample the signal associated with Ti^{3+} defects at 0.7 eV below E_F is clearly observed, indicating higher concentration of these defects in comparison to Cr doped TiO_2 , in which the signal is practically negligible as shown in the Fig. 7(e). However, analyzing in detail the VB spectra of Cr doped samples [inset in Fig. 7(e)], the presence of Ti^{3+} defects can be observed on-resonant conditions as a very weak band. This can explain the observed E_F shift towards the VBM [Fig. 7(a)] as a result of Cr doping, which indicates that a less n-type character can be induced by controlling the Cr concentration⁴¹.

Analysis and comparison to DFT calculations. Theoretical DFT calculations and experimental VB-XPS results acquired on Cr doped TiO_2 have been compared, as shown in Fig. 8(a–c), in which the calculated DOS have been compared to the experimental results from Cr03 sample, and the intensity of the resonant Ti and Cr contributions have been adjusted to fit with the off-resonant VB spectrum.

Among the considered defects, the best fit between experimental VB and calculated data is achieved for the $2\text{Cr} + \text{V}_\text{O}$ defect using the PBE functional. In the calculated combined defect the difference between the pDOS maxima related to Ti(3d) and Cr(3d) states is about 5.5 eV for HSE [Fig. 8(a)], 4.6 eV for PBE [Fig. 8(b)], whereas the experimental difference between the Ti and Cr resonant peaks is about 4.3 eV [Fig. 8(c)]. Thus, the Cr defect states of 3d nature are located within the E_g of TiO_2 . The deviation between the Ti(3d)-Cr(3d) states separation calculated by DOS and experimental VB may be originated by the resultant structural relaxation of the Cr defects⁴², as well as the differences between the DFT model and the measurement conditions of the actual system.

Oxygen defects and other structural defects, such as Ti interstitial, can be found naturally in a real TiO_2 system, and more frequently at the surface^{33,35,43}. According to our DFT results, in order to achieve charge neutrality, Cr atoms could trap electrons from V_O^0 defects and hence be reduced to the most stable oxidation state (Cr^{3+}). Therefore, two Cr defects could be compensated by the creation of a single V_O^0 . The presence of Ti^{3+} defects are related to the presence of V_O^0 , in which two electrons can occupy Ti(3d) states reducing two nearby Ti^{4+} ions^{33,44}. Kim *et al.*⁴⁵ stated that Cr^{3+} defects in rutile TiO_2 are promoted when the samples are grown under oxygen poor conditions and determined that the formation energy of V_O^{2+} and Cr^{3+} is smaller than the formation energy of Cr^{4+} . Taking into account that the formation energy of V_O^{2+} is also smaller than V_O^{1+} and $\text{V}_\text{O}^{0,33,35}$, it is expected that the preferential oxidation state of Cr in TiO_2 should be Cr^{3+} . Thus, a single V_O^0 could be changed into V_O^{2+} by

the reduction of Cr^{4+} ions into Cr^{3+} , leading to higher concentration of coordinated $\text{Cr}^{3+}-\text{V}_\text{O}^{2+}-\text{Cr}^{3+}$ defects and hence reducing the presence of V_O^0 . This is consistent with the observed quenching of the Ti^{3+} related emissions in the luminescence spectra of Cr doped TiO_2 favoring the Cr^{3+} luminescent emissions, reported in previous works^{11,19}. However, experimental VB spectrum shows that the E_F location is about 2.6 eV above the Cr resonant peak, which means that, considering that the E_g of crystalline rutile is about 3.1 eV, the E_F localization is still close to the CB of rutile TiO_2 .

The effect of the crystal field (CF) is directly related to the coordination symmetry of Ti atoms, which implies that the hybridized metal-ligand bonds ($\text{O}(2p)$ orbitals in TiO_2) are very sensitive to local distortions in the rutile lattice³². A complementary study on the CF splitting and tetragonal distortions associated with the presence of Cr in rutile TiO_2 has been also performed by a deeper analysis of the $\text{Ti}-\text{L}_3$ absorption edge. The tetragonal distortion, which is due to the elongation of the apical $\text{Ti}-\text{O}$ bonds, has a strong influence on the $\text{Ti}-\text{L}_{2,3}$ edge features rather than trigonal distortions, which can be neglected in TiO_2 ^{36,38}. This implies that a simplified D_{4h} symmetry is enough to describe the Ti^{4+} ion in the rutile cell³⁸. Figure 8(d) shows the $\text{Ti}-\text{L}_3$ edge for undoped TiO_2 and Cr-doped TiO_2 microtubes (Cr02 and Cr03), where slight variations can be appreciated as the concentration of Cr increases. As aforementioned, Cr incorporation modifies slightly the L_3 edge, and in a greater extent the e_g related band. In this case, by Gauss-Lorentz (G-L) band deconvolution, the L_3 edge can be decomposed into four bands labeled as A, B, C and D. It can be observed in Fig. 8(e) that A and B bands are nearly overlapped for t_{2g} states. Thereby, t_{2g} states are identified by the $A+B$ maximum. C and D bands, located at higher energies and related to the e_g states, show an absolute energy difference $|E_\text{C} - E_\text{D}|$ of about 1 eV. Information related to the crystal environment of Ti ions can be extracted from the G-L deconvolution of experimental Ti L_3 edge, in which $E_\text{D} - E_{A+B}$ could be related to the variations of the CF splitting ($10Dq$) and the difference $|E_\text{C} - E_\text{D}|$ could be associated with variations of the tetragonal distortion parameter defined in absolute value as $|E(b_{1g}) - E(a_{1g})| = |\delta|$ ³⁸.

Figures 8(f,g) show an estimation of the CF splitting ($10Dq$) and the $|\delta|$ parameter as a function of the amount of Cr, in cationic fraction, calculated from the $\text{Ti}-\text{L}_3$ absorption edge corresponding to samples Cr02, Cr03 and samples with variable content of around 4 cat.% and 5 cat.% Cr, composed by sintered grains and precursor powder respectively. In both cases, the CF splitting decreases when Cr dopants are incorporated up to 3 cat.% Cr, and tends to increase when the amount of Cr is above this value. According to our previous results, the Cr solubility limit observed for rutile TiO_2 microtubes grown by vapor-solid method is in the order of 3 cat.% Cr, which could indicate that the Cr defect site in the rutile lattice varies for concentrations either below or above this value. The $|\delta|$ parameter, associated with tetragonal distortion, also presents a slight reduction up to 3 cat.% Cr. Analyzing the calculated atomic coordinates of the Ti and O atoms surrounding the $\text{Cr}_{\text{Ti}}^{1-}$ defect, a tetragonal distortion reduction has been observed in some of the TiO_6 octahedra. The apical (D) and basal (d) $\text{Ti}-\text{O}$ bonds of the in-plane TiO_6 octahedra which are sharing corners with the CrO_6 octahedron are $D = 2.000 \text{ \AA}$ and $d = 1.967 \text{ \AA}$ respectively, so the relative difference $|D - d|/D$ is reduced from 2.4% (bulk rutile TiO_2) to 1.6% using the calculated D and d , indicating a reduction of the tetragonal distortions. This is in agreement with the reduction of the $|\delta|$ parameter calculated by the G-L deconvolution of experimental $\text{Ti}-\text{L}_3$ spectra.

As the local distortions induced by Cr affects directly to the crystal environment of TiO_2 , the physical behavior of the Cr defects should be also dependent on their local environment. The relatively small tetragonal distortion calculated for both Cr_{Ti}^0 and $\text{Cr}_{\text{Ti}}^{1-}$ defects indicates that the CrO_6 octahedra in TiO_2 present O_h symmetry independently of the Cr oxidation state. XAS, XPS and DFT results indicate a predominant Cr^{3+} ion in our system. Previous work¹⁹ reported a characteristic emission related to Cr^{3+} , also called R -lines, using CL spectroscopy as an evidence of the presence of octahedral coordinated Cr^{3+} ions in our Cr-doped TiO_2 microtubes. However, that emission was observed at low temperature ($T = 110 \text{ K}$). Taking into account the energy of the Cr^{3+} characteristic emission (1.79 eV)¹⁹ and the corresponding Tanabe-Sugano diagram for d^3 systems⁴⁶, the minimum crystal field value (Dq) necessary to observe the R -lines is about 1.8 eV. On the other hand, Urusov and Taran⁴⁷ reported the evolution of $10Dq$ as a function of the Cr-O distance ($d_{\text{Cr-O}}$) for a large number of compounds with octahedral coordinated Cr^{3+} ions obtaining the relation $10Dq \propto (d_{\text{Cr-O}})^{-5}$, revealing the high sensitivity of the CF to the local environment. In accordance to our calculated Cr-O distances (1.99–2.00 \AA) and applying a correction factor of 0.99 to arrange the calculations to experimental TiO_2 lattice parameters, the $10Dq$ parameter could vary from 2.05 to 2.12 eV. Therefore, according to the Tanabe-Sugano diagrams, it should be possible to observe the R -lines in Cr-doped TiO_2 . However, the energy separation between Ti^{3+} (0.9 eV below E_F) and Cr^{3+} (2.6 eV below E_F) defect states obtained from the VB spectrum [Fig. 7(e)] is about 1.7 eV. Therefore, the proximity of V_O plays an important role on the recombination process of Cr^{3+} ions in rutile TiO_2 . As the Cr concentration increases the charge neutrality can be achieved by creating Cr^{4+} defects or by inducing V_O that, according to our results, in the most stable structures tends to transfer electrons to the Cr atoms resulting in an increment of V_O^{2+} defects.

Conclusion

In summary, single crystalline Cr doped TiO_2 micro-tubes have been employed as model material to successfully compare theoretical simulations and experimental results on the Cr doping of rutile TiO_2 . As a result, a deeper comprehension on the Cr incorporation in the rutile structure has been obtained. Aspects regarding the incorporation of chromium by forming a complex defect with two Cr atoms and one O vacancy ($2\text{Cr}_{\text{Ti}} + \text{V}_\text{O}$) have been elucidated. The electrons from the oxygen vacancy tend to be localized at the t_{2g} states of the Cr ions in order to reach the stable oxidation state of Cr^{3+} . These results, showing that oxygen defects play a crucial role in the stabilization of Cr^{3+} in the rutile lattice, have been confirmed both theoretically and experimentally, as the separation between the theoretical states due to $\text{Ti}(3d)$ and $\text{Cr}(3d)$, calculated by the pDOS, is in agreement with the one obtained experimentally by XPS resonant measurements. Moreover Cr effects on the crystal field and tetragonal distortion have been studied both from DFT simulations as well as by fitting experimental XAS measurements.

The results indicate a decrease in the value of the $10Dq$ parameter and the tetragonal distortion $|\delta|$ in samples with Cr content lower than 3 cat.%, whereas these parameters increase for samples with higher Cr concentrations. Cr doping of rutile TiO_2 leads to the generation of an energy level 0.55 eV over the VBM of the TiO_2 as obtained by DFT simulations, which is in agreement to the Cr-resonant XPS measurements of the VB. These Cr related shallow levels behave competitively with the Ti^{3+} defect related level, as measured by luminescence and XPS.

References

- Pastore, M., Etienne, T. & De Angelis, F. Structural and electronic properties of dye-sensitized TiO_2 for solar cell applications: from single molecules to self-assembled monolayers. *J. Mater. Chem. C* **4**, 4346–4373 (2016).
- Hussain, M. *et al.* Ag TiO_2 nanocomposite for environmental and sensing applications. *Mater. Chem. Phys.* **181**, 194–203 (2016).
- Fan, X. *et al.* The structural, physical and photocatalytic properties of the mesoporous Cr-doped TiO_2 . *J. Mol. Catal. A Chem.* **284**, 155–160 (2008).
- Tian, B., Li, C. & Zhang, J. One-step preparation, characterization and visible-light photocatalytic activity of Cr-doped TiO_2 with anatase and rutile bicrystalline phases. *Chem. Eng. J.* **191**, 402–409 (2012).
- Yan, K. & Wu, G. Titanium Dioxide Microsphere-Derived Materials for Solar Fuel Hydrogen Generation. *ACS Sustain. Chem. Eng.* **3**, 779–791 (2015).
- Wilke, K. & Breuer, H. D. The influence of transition metal doping on the physical and photocatalytic properties of titania. *J. Photochem. Photobiol. A Chem.* **121**, 49–53 (1999).
- Leedahl, B. *et al.* Study of the Structural Characteristics of 3d Metals Cr, Mn, Fe, Co, Ni, and Cu Implanted in ZnO and TiO_2 — Experiment and Theory. *J. Phys. Chem. C* **118**, 28143–28151 (2014).
- Islam, M. M. & Bredow, T. Rutile Band-Gap States Induced by Doping with Manganese in Various Oxidation States. *J. Phys. Chem. C* **119**, 5534–5541 (2015).
- Da Pieve, F. *et al.* Origin of Magnetism and Quasiparticles Properties in Cr-Doped TiO_2 . *Phys. Rev. Lett.* **110**, 136402 (2013).
- Parks Cheney, C. *et al.* Origins of Electronic Band Gap Reduction in Cr/N Codoped TiO_2 . *Phys. Rev. Lett.* **112**, 36404 (2014).
- Vásquez, G. C. *et al.* Effects of Transition Metal Doping on the Growth and Properties of Rutile TiO_2 Nanoparticles. *J. Phys. Chem. C* **117**, 1941–1947 (2013).
- Vásquez, G. C. *et al.* Influence of Fe and Al doping on the stabilization of the anatase phase in TiO_2 nanoparticles. *J. Mater. Chem. C* **2**, 10377–10385 (2014).
- Matsumoto, Y. *et al.* Structural control and combinatorial doping of titanium dioxide thin films by laser molecular beam epitaxy. in *Applied Surface Science* **189**, 344–348 (2002).
- Wei, Y.-L., Chen, K.-W. & Wang, H. P. Study of Chromium Modified TiO_2 Nano Catalyst Under Visible Light Irradiation. *J. Nanosci. Nanotechnol.* **10**, 5456–5460 (2010).
- Mittal, T., Tiwari, S. & Sharma, S. N. In (eds Jain, V. K., Rattan, S. & Verma, A.) 229–234 (Springer International Publishing, 2017). https://doi.org/10.1007/978-3-319-29096-6_31.
- Santara, B., Imakita, K., Fujii, M. & Giri, P. K. Mechanism of defect induced ferromagnetism in undoped and Cr doped TiO_2 nanorods/nanoribbons. *J. Alloys Compd.* **661**, 331–344 (2016).
- Koohpayeh, S. M., Williams, A. J., Abell, J. S., Lim, J. & Blackburn, E. Cr-doped TiO_2 (rutile): Ferromagnetism in bulk form? *J. Appl. Phys.* **108**, 73919 (2010).
- Kaspar, T. C. *et al.* Negligible magnetism in excellent structural quality $\text{Cr}_x\text{Ti}_{1-x}\text{O}_2$ anatase: Contrast with high-TC ferromagnetism in structurally defective $\text{Cr}_x\text{Ti}_{1-x}\text{O}_2$. *Phys. Rev. Lett.* **95** (2005).
- Vásquez, G. C. *et al.* Cr doped titania microtubes and microrods synthesized by a vapor–solid method. *Cryst Eng Comm* **15**, 5490 (2013).
- Naumkin, A. V., Kraut-Vass, A., Powell, C. J. & Gaarenstroom, S. NIST Standard Reference Database 20 version 4.1. *The National Institute of Standards and Technology NIST 1–49* Available at: <http://srdata.nist.gov/xps> (2012).
- Kresse, G. & Furthmüller, J. Efficiency of ab-initio total energy calculations for metals and semiconductors using a plane-wave basis set. *Comput. Mater. Sci.* **6**, 15–50 (1996).
- Kresse, G. & Furthmüller, J. Efficient iterative schemes for ab initio total-energy calculations using a plane-wave basis set. *Phys. Rev. B* **54**, 11169–11186 (1996).
- Kresse, G. & Hafner, J. Ab initio molecular-dynamics simulation of the liquid-metal–amorphous-semiconductor transition in germanium. *Phys. Rev. B* **49**, 14251–14269 (1994).
- Kresse, G. & Joubert, D. From ultrasoft pseudopotentials to the projector augmented wave method. *Phys. Rev. B* **59**, 1758–1775 (1999).
- Kresse, G. & Hafner, J. Ab initio molecular dynamics for liquid metals. *Phys. Rev. B* **47**, 558–561 (1993).
- Blöchl, P. E. Projector augmented-wave method. *Phys. Rev. B* **50**, 17953–17979 (1994).
- Perdew, J. P., Burke, K. & Ernzerhof, M. Generalized Gradient Approximation Made Simple. *Phys. Rev. Lett.* **77**, 3865–3868 (1996).
- Krukau, A. V., Vydrov, O. A., Izmaylov, A. F. & Scuseria, G. E. Influence of the exchange screening parameter on the performance of screened hybrid functionals. *J. Chem. Phys.* **125**, 224106 (2006).
- Tang, W., Sanville, E. & Henkelman, G. A grid-based Bader analysis algorithm without lattice bias. *J. Phys. Condens. Matter* **21**, 84204 (2009).
- Vásquez, G. C. *et al.* Oxygen vacancy related distortions in rutile TiO_2 nanoparticles: A combined experimental and theoretical study. *Phys. Rev. B - Condens. Matter Mater. Phys.* **94** (2016).
- Momma, K. & Izumi, F. VESTA 3 for three-dimensional visualization of crystal, volumetric and morphology data. *J. Appl. Crystallogr.* **44**, 1272–1276 (2011).
- Stoyanov, E., Langenhorst, F. & Steinle-Neumann, G. The effect of valence state and site geometry on $\text{Ti L}_{3,2}$ and O K electron energy-loss spectra of Ti_xO_y phases. *Am. Mineral.* **92**, 577–586 (2007).
- Janotti, A. *et al.* Hybrid functional studies of the oxygen vacancy in TiO_2 . *Phys. Rev. B* **81**, 85212 (2010).
- Thomas, A. G. *et al.* Comparison of the electronic structure of anatase and rutile TiO_2 single-crystal surfaces using resonant photoemission and x-ray absorption spectroscopy. *Phys. Rev. B* **75**, 35105 (2007).
- Malashevich, A., Jain, M. & Louie, S. G. First-principles DFT + GW study of oxygen vacancies in rutile TiO_2 . *Phys. Rev. B* **89**, 75205 (2014).
- de Groot, F. M. F. *et al.* 2p X-ray absorption of titanium in minerals. *Phys. Chem. Miner.* **19**, 140–147 (1992).
- Drera, G. *et al.* Labeling interacting configurations through an analysis of excitation dynamics in a resonant photoemission experiment: the case of rutile TiO_2 . *J. Phys. Condens. Matter* **25**, 75502 (2013).
- de Groot, F. & Kotani, A. *Core Level Spectroscopy of Solids. Advances in condensed matter science* **6**, (CRC Press, 2008).
- Jiang, B., Zuo, J. M., Jiang, N., O’Keeffe, M. & Spence, J. C. H. Charge density and chemical bonding in rutile, TiO_2 . *Acta Crystallogr. Sect. A Found. Crystallogr.* **59**, 341–350 (2003).
- Luciu, I., Bartali, R. & Laidani, N. Influence of hydrogen addition to an Ar plasma on the structural properties of TiO_{2-x} thin films deposited by RF sputtering. *J. Phys. D. Appl. Phys.* **45**, 345302 (2012).
- Cao, J., Zhang, Y., Liu, L. & Ye, J. A p-type Cr-doped TiO_2 photo-electrode for photo-reduction. *Chem. Commun.* **49**, 3440 (2013).

42. Ebina, T., Iwasaki, T., Chatterjee, A., Katagiri, M. & Stucky, G. D. Comparative Study of XPS and DFT with Reference to the Distributions of Al in Tetrahedral and Octahedral Sheets of Phyllosilicates. *J. Phys. Chem. B* **101**, 1125–1129 (1997).
43. Wendt, S. *et al.* The Role of Interstitial Sites in the Ti3d Defect State in the Band Gap of Titania. *Science* **320**, 1755–1759 (2008).
44. Stausholm-Møller, J., Kristoffersen, H. H., Hinnemann, B., Madsen, G. K. H. & Hammer, B. DFT + *U* study of defects in bulk rutile TiO₂. *J. Chem. Phys.* **133**, 144708 (2010).
45. Kim, R. *et al.* Charge and magnetic states of rutile TiO₂ doped with Cr ions. *J. Phys. Condens. Matter* **26**, 146003 (2014).
46. Tanabe, Y. & Sugano, S. On the absorption spectra of complex ions II. *J. Phys. Soc. Japan* **9**, 766–779 (1954).
47. Urusov, V. S. & Taran, M. N. Structural relaxation and crystal field stabilization in Cr³⁺-containing oxides and silicates. *Phys. Chem. Miner.* **39**, 17–25 (2012).
48. Crocombette, J. P. & Jollet, F. Ti 2p X-ray absorption in titanium dioxides (TiO₂): the influence of the cation site environment. *J. Phys. Condens. Matter* **6**, 10811–10821 (1994).
49. Diebold, U. The surface science of titanium dioxide. *Surf. Sci. Rep.* **48**, 53–229 (2003).
50. Amtout, A. & Leonelli, R. Optical properties of rutile near its fundamental band gap. *Phys. Rev. B* **51**, 6842–6851 (1995).
51. Park, S.-G., Magyar-Köpe, B. & Nishi, Y. Electronic correlation effects in reduced rutile TiO₂ within the LDA + *U*. *Phys. Rev. B* **82**, 115109 (2010).

Acknowledgements

This work was supported by MINECO/FEDER (Projects No. MAT 2015-65274-R and MAT2016- 81720-REDC), NILS Project (008-ABELCM-2013), Notur Project No. nn4608k, and HyMatSiRen No. project272806 from the Research Council of Norway.

Author Contributions

G.C.V. wrote the manuscript, data analysis and figures. S.Zh.K. and G.C.V. designed and performed DFT calculations. J.R.-C. and G.C.V. synthesized the materials. A.C., D.M., G.C.V., E.M. and S.N. performed XPS and XAS measurements. A.C., D.M. and G.C.V. designed the experiments. A.C., D.M. and S.Zh.K. supervised the project. All the authors discussed the results and corrected the manuscript.

Additional Information

Supplementary information accompanies this paper at <https://doi.org/10.1038/s41598-018-26728-3>.

Competing Interests: The authors declare no competing interests.

Publisher's note: Springer Nature remains neutral with regard to jurisdictional claims in published maps and institutional affiliations.



Open Access This article is licensed under a Creative Commons Attribution 4.0 International License, which permits use, sharing, adaptation, distribution and reproduction in any medium or format, as long as you give appropriate credit to the original author(s) and the source, provide a link to the Creative Commons license, and indicate if changes were made. The images or other third party material in this article are included in the article's Creative Commons license, unless indicated otherwise in a credit line to the material. If material is not included in the article's Creative Commons license and your intended use is not permitted by statutory regulation or exceeds the permitted use, you will need to obtain permission directly from the copyright holder. To view a copy of this license, visit <http://creativecommons.org/licenses/by/4.0/>.

© The Author(s) 2018